Check for updates

Simple and robust phenoxazine phosphonic acid molecules as self-assembled hole selective contacts for high-performance inverted perovskite solar cells†

Zhaoning Li,‡ Qin Tan,‡ Guocong Chen, Han Gao, Jiafeng Wang, Xusheng Zhang, Jingwei Xiu, Wei Chen and Zhubing He ⬡ *

For inverted perovskite solar cells (PSCs), the interfacial defects and mismatched energy levels between the perovskite absorber and charge-selective layer restrain the further improvement of photovoltaic performance. Interfacial modification is a powerful tool for defect passivation and energy level turning by developing new charge-selective materials. Herein, we report three new molecules, 2BrCzPA, 2BrPTZPA, and 2BrPXZPA as self-assembled hole selective contacts (SA-HSCs) by an economical and efficient synthetic procedure. Benefiting from the stronger electron-donating ability of phenothiazine and phenoxazine compared to that of carbazole, 2BrPTZPA and 2BrPXZPA showed more matched energy levels and decreased energy loss. In addition, the ITO substrate coated with 2BrPTZPA and 2BrPXZPA could induce higher-quality perovskite crystal growth without obvious grain boundaries in the vertical direction. Consequently, the corresponding inverted PSCs with decreased trap state density achieved high power convention efficiencies (PCEs) of 22.06% and 22.93% (certified 22.38%) for 2BrPTZPA and 2BrPXZPA, respectively. Furthermore, the 2BrPXZPA-based device with encapsulation retained 97% of the initial efficiency after 600 h of maximum power point tracking under one sun continuous illumination. Finally, 2BrPXZPA was also used for the surface modification of NiO_x, and the inverted PSC based on the NiO_x/2BrPXZPA bilayer achieved a higher PCE of 23.66% with an open circuit voltage of 1.21 V. This work extends the design strategy of SA-HSCs for efficient and stable inverted PSCs and promotes the commercialization process.

1. Introduction

Over the last decade, organic–inorganic hybrid perovskite solar cells (PSCs) have experienced impressive progress and shown great potential in commercialization. The power conversion efficiency (PCE) of PSCs has increased from 3.8% to 25.7% with a conventional normal (n-i-p) device structure.[1–3] Simultaneously, the inverted (p-i-n) structure PSCs have also been developed rapidly owing to their unique merits in contrast to the normal ones, such as a simpler device structure, more facile fabrication process, and hence lower cost and easily adapting to tandem solar cells.[4–6] However, the

Department of Materials Science and Engineering, Institute of Innovative Materials (I2M), Shenzhen Key Laboratory of Full Spectral Solar Electricity Generation (FSSEG), Southern University of Science and Technology, No. 1088, Xueyuan Rd, Shenzhen, 518055 Guangdong, China. E-mail: hezb@sustech.edu.cn
†Electronic supplementary information (ESI) available. See DOI: https://doi.org/10.1039/d2nr05677a
‡These authors contributed equally to this work.

maximum PCE of inverted PSCs (~25%)[7] still lags behind their conventional counterparts, predominantly due to a relatively lower open-circuit voltage (V_{oc}) and fill factor (FF). Therefore, the interface between perovskite and the charge-selective layers should be carefully managed to reduce energy loss resulting from carrier recombination. Compared to the top electron selective contact (ESC) between perovskite and the metal electrode, the post-treatment and modification of the buried interface are more difficult. As such, an ideal hole selective contact (HSC) is needed for achieving efficient and stable inverted PSCs. The ideal hole selective materials (HSMs) should meet the following requirements: (i) extract and transport holes from the perovskite to anode, (ii) improve the energy-level alignment to reduce energy loss by recombination, and (iii) reduce interfacial defect density and induce the nucleation and high-quality growth of the above perovskite films.[8–10] Besides, HSMs in the inverted PSCs should keep structure stability under light soaking and heat damping without the degradation of both transmittance and charge transport. Although some materials have been employed as

HSMs, including popular materials such as NiO_x,[11–14] PTAA,[15,16] and PEDOT:PSS,[17,18] rationally designed molecules are still necessary to meet the above-mentioned requirements. For example, some rationally-designed organic semiconductors with the D–A–D structure were reported by our group and other colleagues, obtaining a good device performance.[19–22] However, those molecules seem complex and of high synthesis cost, undermining their utilization in future mass production. Moreover, HSMs should preferably have functional groups to anchor both the perovskite and ITO, enabling interfacial passivation and inducing high-quality growth of the perovskite film.

Recently, carbazole (Cz) based small molecules with phosphonic acid (PA) groups have been used as self-assembled hole selective contacts (SA-HSCs) to replace the conventional HSCs in inverted PSCs. These molecules consist of three critical parts: PA-based anchoring group, alkyl chain linker, and Cz-based donor backbone with alternating substituent functional groups. In 2018, Magomedov et al. reported for the first time PACz with dimethoxy diphenylamine substituent groups, named V1036,[23] that can be easily self-assembled as HSCs in an inverted planar PSC, achieving a PCE of 17.98% (Fig. 1a). After that, various kinds of PACz derivatives with different substituent groups were developed as SA-HSCs, such as 2PACz, MeO-2PACz, and Me-4PACz, as shown in Fig. 1a,[24,25] and more PACz series molecules could be found in Fig. S1.† Because the PACz-based molecules are small, chemically stable and easily deposited, they have also been popularly utilized in such tandem solar cells as perovskite/silicon,[25] perovskite/perovskite[26] and perovskite/organic.[27] PACz-based molecules show huge potential in hole extraction and defect passivation at the interface between perovskite and ITO films. Molecular engineering would play a crucial role in further enhancing the hole

selective function for the PACz series, especially on the substituent groups. Besides, atom doping is widely employed to modulate the electronic structure of organic molecules along with grafting specified side groups. As Fig. 1b shows, phenothiazine (PTZ) and phenoxazine (PXZ), can be considered as typical examples by doping S and O atoms in Cz, respectively. They have been widely applied to construct organic dyes and emitters used in dye-sensitized solar cells[28,29] and organic light-emitting diodes.[30–32] Later on, PTZ and PXZ were also used as the donor unit to construct HSMs with A–D–A or D–π–D structures without the PA group for inverted PSCs, achieving good device performances.[33–35] Recently, Zhu et al. modified PTZPA by grafting 4,4′-dimethoxytriphenylamine along with extending the length of the alkyl chain to hexyl (named as TPT-P6), achieving an excellent PCE of 21.43%.[36] On the other hand, Hong et al. grafted Br at the side site of PTZPA with ethyl (named Br-2EPT) and obtained a remarkable PCE of 22.44% (certified 21.81%).[37] The above two reports demonstrated that S atoms containing PTZPAs can effectively modulate their highest occupied molecule orbital (HOMO) levels and herein enhance the hole-extraction in a device, accounting for the efficient inverted PSCs along with the passivation effect of S by coordinating with Pb^{2+} from perovskites. More than those effects, the alkyl chain, and the substitute group affect the molecular configuration in space and herein their stacking form in the self-assembled film, which can also influence the above interfacial interactions in the device. Moreover, as an analogue of PTZPA, the potential application of PXZPA with O atom doped was fully ignored in PSCs although O has stronger coordination with Pb than S. In addition, a simple structural molecule is inclined to be robust and adapted to mass production and large-scale process.

Regarding the above concerns, in this study, we designed and synthesized a simple structure 2BrPXZPA with a doped O atom, bromine-substituted groups and a butyl chain as the spacer linker. For comparison, 2BrCzPA and 2BrPTZPA were also synthesized. Their molecule structures are shown in Fig. 1b. Besides the doping of the O atom, the butyl chain was used as a suitable spacer linker to optimize the stacking of molecules,[25] along with improved synthetic yield while bromine was expected to tune its electronic structure for band alignment between 2BrPXZPA and perovskites and naturally coordinating the exposed Pb^{2+} from perovskites.[34] Depending on the rational design discussed above, the synthesized 2BrPXZPA has a suitable energy level and matches better with the involved perovskite film compared to 2BrPTZPA. Based on 2BrPXZPA, we obtained the impressive champion device PCE of 22.93% along with 22.38% certified, which beat the current record of the inverted devices employing small molecules as HSMs.[38] In comparison, 2BrPTZPA-based devices also present excellent performance with a superior PCE of 22.06% although it is inferior to that of 2BrPXZPA. Whereas, 2BrCzPA without doping with any atom shows poor device performance. As expected for robust small molecules, the 2BrPXZPA-based device shows competitive long-term stability with 97% of the initial efficiency retained after 600 hours of light soaking
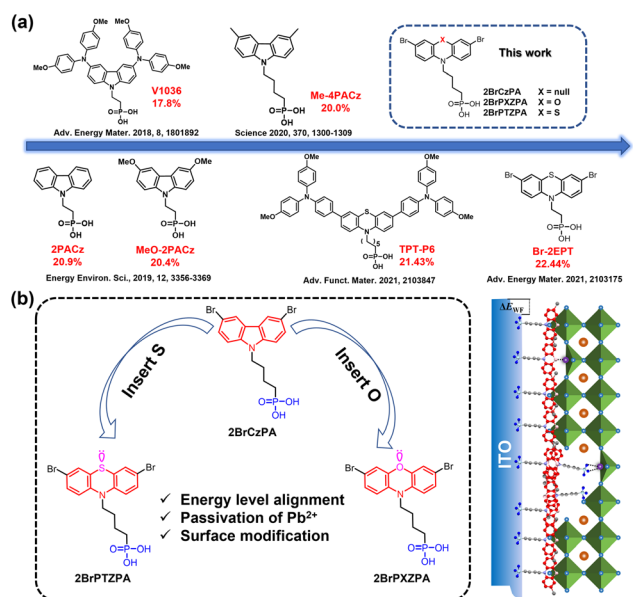

Fig. 1 (a) Recent development of phosphoric acid-based self-assembled hole-selective materials for inverted perovskite solar cells. (b) Molecular design strategy and chemical structures reported in this work.

under one standard sun illumination (AM 1.5G). Furthermore, when we modified the NiO_x HSMs layer with 2BrPXZPA, a superior PCE of 23.66% was achieved, obviously improved from 20.55% of the control NiO_x-based device. Systematic device-physics characterizations were conducted to explore the mechanism behind these along with a detailed exploration of their intrinsic properties.

2. Experimental

2.1. Materials

2.1.1. Materials for synthesis. Unless otherwise mentioned, chemicals for the synthesis were purchased from Bide Pharmatech Ltd, Energy Chemical Ltd, J&K Scientific Ltd, and Aladdin (Shanghai) Ltd and used as received without further purification.

2.1.2. Materials for device fabrication. *N,N*-Dimethylformamide (DMF), dimethyl sulfoxide (DMSO), chlorobenzene (CB), and cesium iodide (CsI) were purchased from Sigma-Aldrich (Shanghai, China). Lead(II) iodide (PbI_2) and lead(II) bromide ($PbBr_2$) were purchased from TCI. Methylammonium bromide (MABr) and formamidinium iodide (FAI) were purchased from Greatcell Solar. $PC_{61}BM$ was purchased from Daeyeon Chemicals. All materials above were used as received.

2.2. Device fabrication

The inverted (p-i-n) perovskite solar cell studied in this work with a configuration of ITO/SA-HSCs/perovskite/$PC_{61}BM$/BCP/Ag. The ITO glass substrate was cleaned successively with detergent (2% in deionized water), deionized water, acetone, and isopropanol, each for 20 minutes in an ultrasonic bath. Afterward, the substrate was dried with N_2 and activated with UV–ozone (15 min) for the device fabrication. 2BrCzPA, 2BrPTZPA, and 2BrPXZPA with a concentration of 1 mg mL^{-1} in THF were spin-coated on the cleaned ITO substrate and annealed at 100 °C for 10 min. The $Cs_{0.05}(FA_{0.85}MA_{0.15})_{0.95}Pb(I_{0.85}Br_{0.15})_3$ perovskite (labeled as CsFAMA) precursor solution was prepared according to our previous report.[39] The CsFAMA perovskite films were prepared by spin coating the precursor solution (1.3 M, 1000 rpm, 10 s/5000 rpm, 25 s), at the last 20 s of the procedure, the film was treated with 300 μL CB and then annealed at 100 °C for 60 min. $PC_{61}BM$ (2 wt% in CB) was spin-coated on a perovskite layer and annealed at 100 °C for 10 min. Then, the substrate was transferred into a high vacuum thermal evaporator, the BCP (8 nm) and Ag (100 nm) were subsequently evaporated. For the NiO_x/2BrPXZPA-based bilayer device, the NiO_x layer was prepared by spin coating NiO_x nanoparticle solution (20 mg mL^{-1} in deionized water, 4000 rpm, and 40 s) and annealed at 110 °C for 10 min before the deposition of 2BrPXZPA. The space charge limited current (SCLC) method was used to evaluate the trap-state density in the perovskite films. The dark *I–V* curves of the hole-only devices using the structure consisting of ITO/NiO_x/SA-HSCs/perovskite/spiro-OMeTAD/Au.

2.3. Materials and devices characterization

NMR spectra were recorded on Bruker Avance 500 and Bruker Avance 400 spectrometers in $CDCl_3$ and DMSO-d_6. High-resolution mass spectra (HRMS) were recorded on a Thermo Scientific Q Exactive mass spectrometer, using electrospray ionization (ESI) as the ionization mode. Thermal gravimetric analysis (TGA) was recorded on a Mettler TGA1 with a heating rate of 10 °C min^{-1} under nitrogen flow. Cyclic voltammetry (CV) was recorded on a CHI620E voltammetric analyzer with a scan rate of 50 mV s^{-1}. Tetra-*n*-butylammonium hexafluorophosphate was used as the electrolytes, an Ag/AgCl electrode as the reference electrode, a platinum wire as the counter electrode, and a glassy carbon electrode as the working electrode. UV-vis spectra of the three synthesized compounds in THF (1×10^{-5} M) and films spin-coated on quartz were recorded on a PerkinElmer Lambda 950 spectrometer. The steady-state and time-resolved PL spectra were measured using a spectrofluorometer (FS5, Edinburgh Instruments), and a 405 nm pulsed laser was used as the excitation source for the measurement. Top-view morphology and cross-section SEM were characterized using the HITACHI SU8230 instrument. X-ray photoelectron spectroscopy (XPS) measurements were carried out using an Omicron ESCA Probe XPS spectrometer (Thermo Scientific ESCALAB 250Xi) using 150 eV pass energy and 1 eV step size for the survey scan and 20 eV pass energy and 0.01 eV step size for the fine scan. To measure work function, ultraviolet photoelectron spectroscopy (UPS) spectra were recorded using an imaging photoelectron spectrometer (Axis Ultra, Kratos Analytical Ltd), with a non-monochromated He Iα photon source (h_ν = 21.22 eV). Au is a reference. Contact angle measurements were performed using a KLA-Tencore D120 surface profiler.

J–V measurements were carried out using a Keithley 2400 source meter in the ambient environment at ~25 °C and ~45% RH. The devices were measured both in reverse scan (1.2 V → −0.2 V, step 0.02 V) and forward scan (−0.2 V → 1.2 V, step 0.02 V) with a 10 ms delay time. The illumination was provided with an Oriel Sol3A solar simulator with AM 1.5G spectrum and a light intensity of 100 mW cm^{-2} was calibrated using a standard KG-5 Si diode. The active area (0.08 cm^2) of our device was calibrated with a shadow mask during the measurements. EQE measurements for the devices were conducted using an Enli-Tech (Taiwan) EQE measurement system. The long-term operational stability in this work was conducted by applying the encapsulated devices under 1 sun equivalent LED lamp in an ambient environment (~25 °C and ~50% RH). The maximum power point was recorded every minute. The 2BrPXZPA-based PSC was certified at an independent lab (SIMIT, Shanghai, Chinese Academy of Sciences).

3. Results and discussion

Based on the above design principles of SA-HSCs, the C–C bond between two benzenes in 3,6-dibromocarbazole was cleaved and a heteroatom of O or S was inserted to obtain PXZ

or PTZ-based SA-HSCs, (4-(3,7-dibromo-10H-phenothiazin-10-yl)butyl)phosphonic acid (2BrPTZPA) and (4-(3,7-dibromo-10H-phenoxazin-10-yl)butyl)phosphonic acid (2BrPXZPA), as shown in Fig. 1b. (4-(3,6-Dibromo-9H-carbazol-9-yl)butyl)phosphonic acid (2BrCzPA) with the functional group of 3,6-dibromocarbazole were also synthesized as a reference in this study. The synthetic details of the three SA-HSCs are available in the ESI, Scheme S1.† Firstly, PTZ and PXZ reacted with 1,4-dibromobutane to produce the intermediates PTZC4Br and PXZC4Br, respectively. Then, N-bromosuccinimide (NBS) was used for bromination in dichloromethane at room temperature to produce 2BrPTZC4Br and 2BrPXZC4Br. In the next step, a name reaction of Michaelis–Arbuzov phosphonate synthesis was used to get the corresponding sulphosuccinic acid ester. Finally, the sulphosuccinic acid ester was hydrolyzed with bromotrimethylsilane, methanol, and water to produce the final products 2BrPTZPA and 2BrPXZPA. The synthesis of 2BrCzPA was started from 3,6-dibromocarbazole following a procedure similar to the one mentioned above. The chemical structures of three compounds were verified by a combination of ^{1}H, ^{13}C, and ^{31}P nuclear magnetic resonance (NMR) spectroscopy (Fig. S17–S35†), high-resolution mass spectroscopy (HRMS, Fig. S36–S38†), and elemental analysis. The synthesis cost was carefully calculated following a previously reported method[40] and shown in Schemes S2–S4 and Tables S1–S3.† The most expensive compound with the outstanding performance of three new materials was 2BrPXZPA (15.51 $ per g), higher than that of 2BrPTZPA (7.96 $ per g) and 2BrCzPA (6.18 $ per g), while only about one percent of the commonly used PTAA (1568 $ per g) in inverted PSCs. The low-cost hole selective materials will be more competitive for the industrialization of PSCs in the future.

Density functional theory (DFT) was first used to simulate the molecularly optimized chemical structures, electron cloud density of frontier orbitals, and the electronic surface potential (ESP) with the B3LYP method and the 6-311G* base set. As shown in Fig. S2,† all three molecules present similar optimized configurations from the top and side views. Notably, the different atomic radii of S and O leading to the intramolecular dihedral angles of PTZ and PXZ were 26.53° and 2.90°, respectively, as shown in Fig. S3.† The highest occupied molecular orbital (HOMO) and lowest unoccupied molecular orbital (LUMO) were both mainly located at the conjugated part and the HOMO was partially extended to the alkyl chain. Benefiting from the lone pair electrons of S and O atoms, dibromophenothiazine, and dibromophenoxazine possessed stronger electron-donating properties compared to those of dibromocarbazole, and leading to higher HOMO energy levels. 2BrPXZPA had the highest HOMO of −5.22 eV, followed by 2BrPTZPA with a little deeper HOMO of −5.34 eV, and 2BrCzPA with a much deeper HOMO of −5.81 eV, which was probably too deep to match with the valence band maximum (VBM) of the perovskite. Besides, the lone pair of electrons of S and O would passivate the perovskite by coordination with exposed Pb^{2+} ions on the subsurface of the perovskite layer.[41] In the electrostatic surface potential (ESP) of molecules, the

red area, and blue area indicated negative and positive potential, respectively. Obviously, apart from the S and O with lone pair electrons, the bromine atoms on the phenyl ring as a Lewis base was anticipated to efficiently passivate the perovskite.[34] For SA-HSCs, the electronic dipole moment of molecules would change the work function of the ITO substrate efficiently.[42,43] To estimate the ability of the three new materials for work function turning, a gas phase dipole moment calculation using DFT was performed, and phosphate groups were replaced by hydrogen atoms by following the reported method.[24,44] The electronic dipole moments of 2BrCzPA, 2BrPTZPA, and 2BrPXZPA with the same direction toward the alky chain were 4.70 D, 3.89 D, and 4.11 D, respectively (Fig. S4†).[45,46] Hence, the work function (WF) of ITO with SA-HSCs would be increased because of the permanent dipole moment layers.

Thermal stability is a basic property for evaluating new materials and would affect the operational stability of PSCs. In this study, thermal gravimetric analysis (TGA) was used to estimate the stability of the three new materials with the thermal decomposition temperature (T_d, 5% weight loss) and the thermal gravimetric curve is shown in Fig. S6.† The T_d of 2BrCzPA, 2BrPTZPA and 2BrPXZPA were 264 °C, 234 °C and 225 °C, respectively. Differential scanning calorimetry (DSC) was also performed, however, there was no evident endothermic peak for the glass transition process in the DSC trace. All of these represented good thermal stability, much higher than the processing and working temperature of PSC devices.

The photophysical properties of the three SA-HSMs were carefully evaluated. As shown in Fig. 2a and Table 1, the UV-vis absorption spectra of the three SA-HSMs in the dilute solution (10^{-5} M) of THF represented similar π–π* absorption properties with peaks at 304, 349, and 363 nm for 2BrCzPA, 319 nm for 2BrPTZPA, and 334 nm for 2BrPXZPA. To better understand the absorption properties of these new materials, time-dependent DFT (TD-DFT) was applied to simulate the vertical excitation energy, and the absorption spectra were plotted (Fig. S5†) with B3LYP/6-311G*. For thin films, the absorption peaks of the three materials were slightly red-shifted because of the J-aggregation. The optical band gap (E_g^{opt}) of three materials was estimated from their absorption onset wavelength of films by the equation of $E_g^{opt} = 1240/\lambda_{onset}$ (eV). As shown in Table 1, the E_g^{opt} values of 2BrCzPA, 2BrPTZPA, and 2BrPXZPA were 3.30 eV, 3.25 eV, and 3.16 eV, respectively. In addition, benefitting from the negligible absorption in the visible region of the three new molecules, they exhibited excellent transparency as shown in Fig. 2b, which is salutary for light utilization of PSC devices.

The energy-level match between the HOMO of SA-HSMs and VBM of the perovskite is a basic requirement for decreasing the charge recombination at the interface and achieving high photovoltaic performance. In this study, cyclic voltammetry (CV) was first used to evaluate the energy level of new materials, as shown in Fig. 2c. CV was performed in THF solution with tetrabutylhexafluorophosphate as the electrolyte and ferrocene/ferrocenium as an external reference. A quasi-revers-
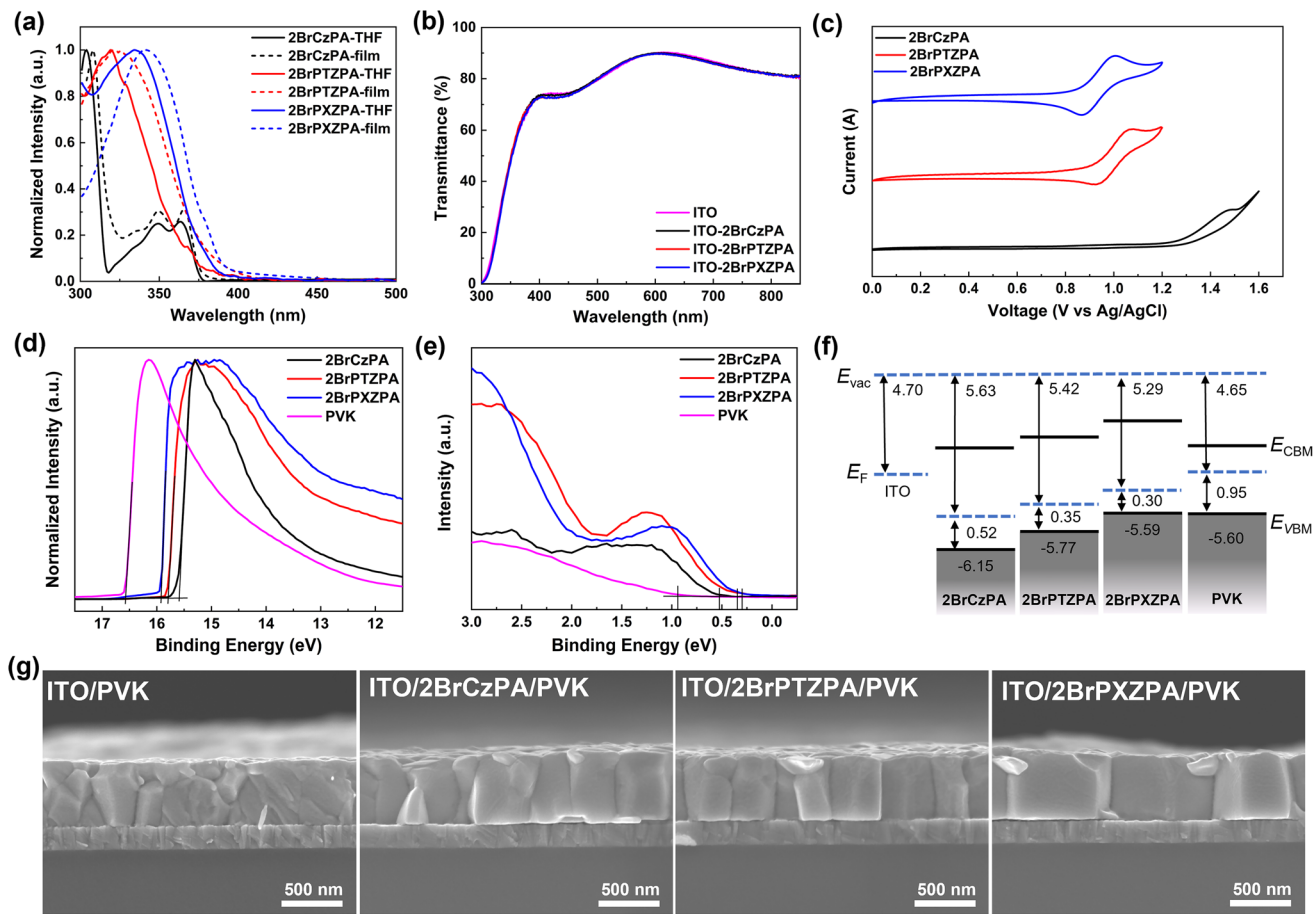
Fig. 2 Optical and electrochemical properties of SA-HSMs. (a) UV-vis absorption spectra of the three SA-HSMs in THF solution (1×10^{-5} mol L^{-1}). (b) Transmittance spectra of ITO and ITO with SA-HSMs. (c) Cyclic voltammograms of three SA-HSMs recorded in THF solution using the Fc/Fc$^+$ as the external reference with a scanning rate of 100 mV s^{-1}. UPS spectra in the (d) cut-off region and (e) on-set region of the perovskite and three SA-HSMs. (f) Energy-level alignment of ITO, perovskite, and three SA-HSMs. (g) Cross-section SEM of PSCs with different substrates.

Table 1 Optical, electrochemical, and thermal properties

	$\lambda_{\text{abs,sol}}{}^a$ (nm)	$\lambda_{\text{abs,film}}$ (nm)	$E_g^{\text{opt}\ b}$ (eV)	HOMO^c (eV)	HOMO^d (eV)	HOMO^e (eV)	T_d (°C)	μ^f (D)
2BrCzPA	363, 349, 304	366, 349, 308	3.30	−5.88	−6.15	−2.85	264	5.02
2BrPTZPA	319	324	3.25	−5.51	−5.77	−2.52	234	3.89
2BrPXZPA	334	342	3.16	−5.46	−5.59	−2.43	225	4.11

^{a} Measured in THF solution with a concentration of 1×10^{-5} mol L^{-1}. ^{b} Estimated from the absorption edge of onset in the neat film using the equation: $E_g^{\text{opt}} = 1240/\lambda_{\text{onset}}$ (eV). ^{c} $E_{\text{HOMO}} = -5.1 - (E_{\text{ox}} - E_{\text{Fc/Fc}^+})$ (eV). ^{d} Estimated from the UPS using the equation $E_{\text{HOMO}} = 21.22 - (E_{\text{cut-off}} - E_{\text{onset}})$ eV. ^{e} $E_{\text{LUMO}} = E_{\text{HOMO}} + E_g^{\text{opt}}$ (eV), where E_{HOMO} was obtained from UPS. ^{f} Dipole moment calculated by DFT based on B3LYP/def2-SVP.[24]

ible oxidation peak could be observed clearly on the CV curves of 2BrPTZPA and 2BrPXZPA, and the HOMO energy level could be calculated as −5.51 eV and −5.46 eV, respectively. However, the oxidation peak of 2BrCzPA was not reversible because of the electrocoupling activity of carbazole. The HOMO energy level of 2BrCzPA was −5.88 eV, which is much lower than that of 2BrPTZPA and 2BrPXZPA.

To better understand the electrochemical properties of materials in the solid state, the UPS was used to measure the HOMO energy levels of the films, as shown in Fig. 2d, e, and

Table 1. The HOMO energy level of 2BrCzPA, 2BrPTZPA, and 2BrPXZPA were calculated as −6.15 eV, −5.77 eV, and −5.59 eV, respectively, which were in the same trend as per the DFT calculations and CV measurements. Notably, 2BrPXZPA with a HOMO energy level of −5.59 eV was the most comparable with the VBM (−5.60 eV) of perovskite, as shown in Fig. 2f, the small energy offset of 0.01 eV indicates that holes could be extracted from the perovskite efficiently and lead to a small voltage loss at the interface. However, the S-containing analog of 2BrPTZPA with a little deeper HOMO than the perovskite

because of the weaker electron-donating property of phenothiazine, and the mismatched energy level might suppress the hole extraction process. What is worse, the HOMO of 2BrCzPA was too deep to permit hole extraction and transportation.

Because of the different electronic dipole moments of the three new molecules, the work function of ITO (4.70 eV) coated by 2BrCzPA, 2BrPTZPA, and 2BrPXZPA was increased to 5.63 eV, 5.42 eV, and 5.29 eV, respectively. The Kelvin probe method[45,47] also was used to confirm the work function of the modified ITO (Fig. S7†), with 5.65 eV, 5.37 eV, and 5.31 eV for 2BrCzPA, 2BrPTZPA, and 2BrPXZPA, respectively, which were almost the same as the UPS result. Before coating by molecules, the bare ITO contact with perovskite results in a lightly downward band bending, as shown in Fig. S8,† and leads to a large hole extraction barrier (ΔE_h = 0.90 eV). Therefore, the PSCs without HSCs would present a very poor photovoltaic performance. In contrast, the modified ITO with enlarged WF would generate a strong downward band bending when in contact with perovskite and decreased the ΔE_h to 0.18 eV and 0.31 eV for 2BrPTZPA and 2BrPXZPA, respectively, which is conducive to the hole extraction at the ITO/perovskite interface. What is more, the downward band bending would also benefit electron blocking because of the increased electron transfer barrier (ΔE_e). However, the ITO was modified by 2BrCzPA with the largest WF of 5.63 eV, which was even deeper than the VBM of perovskite. The mismatched energy level at the interface leading to the hole extraction process from the perovskite to the electrode became more difficult.

The SA-HSMs were deposited on the ITO substrate by a spin-coating method, and the atomic species were studied by X-ray photoelectron spectroscopy (XPS), as shown in Fig. S9.† Compared to the bare ITO, the ITO with SA-HSMs represented the P 2p peak at 133.5 eV and N 1s peak at 399.8 eV, indicating the successful modification. Besides, the In 3d and Sn 3d peaks of ITO with SA-HSMs shifted to a higher binding energy area and showed decreased intensity, which meant that the ITO substrates were covered by a thin layer of molecules.[42]

The wettability of substrates would affect the crystallization process and crystal quality of perovskite, then further influenced the photovoltaic performance of PSCs. In this work, the contact angle of bare ITO and ITO with SA-HSMs was measured, as shown in Fig. S10 and Table S4.† 2BrPTZPA and 2BrPXZPA showed similar hydrophobicity with a water contact angle of 74.20 ± 1.02° and 72.46 ± 0.90°, respectively, because of their almost similar chemical structures with a little difference of S and O in the terminal group. As expected, the water contact angle of 2BrCzPA with 80.73 ± 1.35° was a little higher than that of the two analogues. Compared to the bare ITO with ozone treatment (4.43 ± 0.22°), the enhancement of hydrophobicity indicated that a highly-oriented molecular arrangement with a hydrophilic phosphate group pointing toward the ITO substrate was formed. To further study the surface properties of the three SA-HSMs, the n-hexadecane contact angle was also recorded and the Owens–Wendt method was used to calculate the surface energy of ITO and the three materials. The total

surface energy of ITO, 2BrCzPA, 2BrPTZPA, and 2BrPXZPA were estimated as 73.02, 33.59, 36.76, and 37.69 mJ m^{-2}, respectively. The substrate coated by 2BrPXZPA with surface energy closer to that of perovskite film indicated better compatibility than the other two molecules. However, the ozone-treated bare ITO with the highest surface energy and best hydrophilicity might lead to a fast crystallization process and generate smaller size crystal grains. To ensure the above speculation, scanning electron microscopy (SEM) was used for perovskite film characterization. As shown in Fig. S11 and S12,† the perovskite crystal grains on the modified ITO substrate with a much larger size than the bare ITO substrate. The statistical grain sizes of perovskite crystals on ITO, ITO/2BrCzPA, ITO/2BrPTZPA, and ITO/2BrPXZPA were 155 ± 49 nm, 209 ± 62 nm, 218 ± 76 nm, and 220 ± 61 nm, respectively. The cross-section SEM of the perovskite on bare ITO showed multiple grains with a boundary in the vertical direction, as shown in Fig. 2g, which would effectively impede the charge transfer and result in decreased device performance. After coating with SA-HSMs, the crystal grain size of the perovskite was increased and there was almost no grain boundary in the vertical direction, especially for the ITO/2BrPXZPA substrate. Combining the surface energy results, the SA-HSMs coated on ITO would effectively enhance the crystallization process to obtain crystal grains with larger sizes and fewer boundaries, which would decrease the energy loss of the charge transport and lead to a high short-circuit current (J_{sc}).

To evaluate the photovoltaic performance of three molecules as SA-HSCs in PSCs, a device based on CsFAMA mixed cation perovskite with a configuration of ITO/SA-HSCs/CsFAMA/PC$_{61}$BM/BCP/Ag was fabricated, as shown in Fig. 3a. The CsFAMA was prepared by a one-step anti-solvent method following our previous report,[19] and the SA-HSCs was deposited by spin coating with an optimized concentration of 1 mg mL^{-1} (Fig. S13†). The J–V curves and parameters of the best devices are shown in Fig. 3b and Table 2. The PSC device without SA-HSCs exhibited a very poor photovoltaic performance with a PCE of 4.37% only, which resulted from the unmatched energy level and ineffective hole-extraction between ITO and the perovskite interface. Encouragingly, the 2BrPTZPA-based PSC achieved a high PCE of 22.06% with a J_{sc} of 23.36 mA cm^{-2}, a V_{oc} of 1.18 V, and a FF of 80.02%. Its O-containing analog 2BrPXZPA-based device achieved better performance with a J_{sc} of 23.59 mA cm^{-2}, a V_{oc} of 1.19 V, and a FF of 81.69%, leading to a surprisingly high PCE of 22.93% (citified PCE of 22.38% by Shanghai Institute of Microsystem and Information Technology on December 31st, 2021, Fig. S14†). Furthermore, the PSC devices that used 2BrPTZPA and 2BrPXZPA as SA-HSCs showed negligible hysteresis with a hysteresis index (HI) of 0.006 and 0.002, respectively. The commercial hole-transporting material PTAA-based inverted PSCs was also fabricated as a reference and the photovoltaic performance is shown in Fig. S15.† The winning device of PTAA-based PSC showed a V_{oc} of 1.19 V, a J_{sc} of 22.57 mA cm^{-2}, a FF of 81.48%, and a high PCE of 21.88% was achieved. Notably, 2BrPTZPA and 2BrPXZPA-based devices both exhibited higher
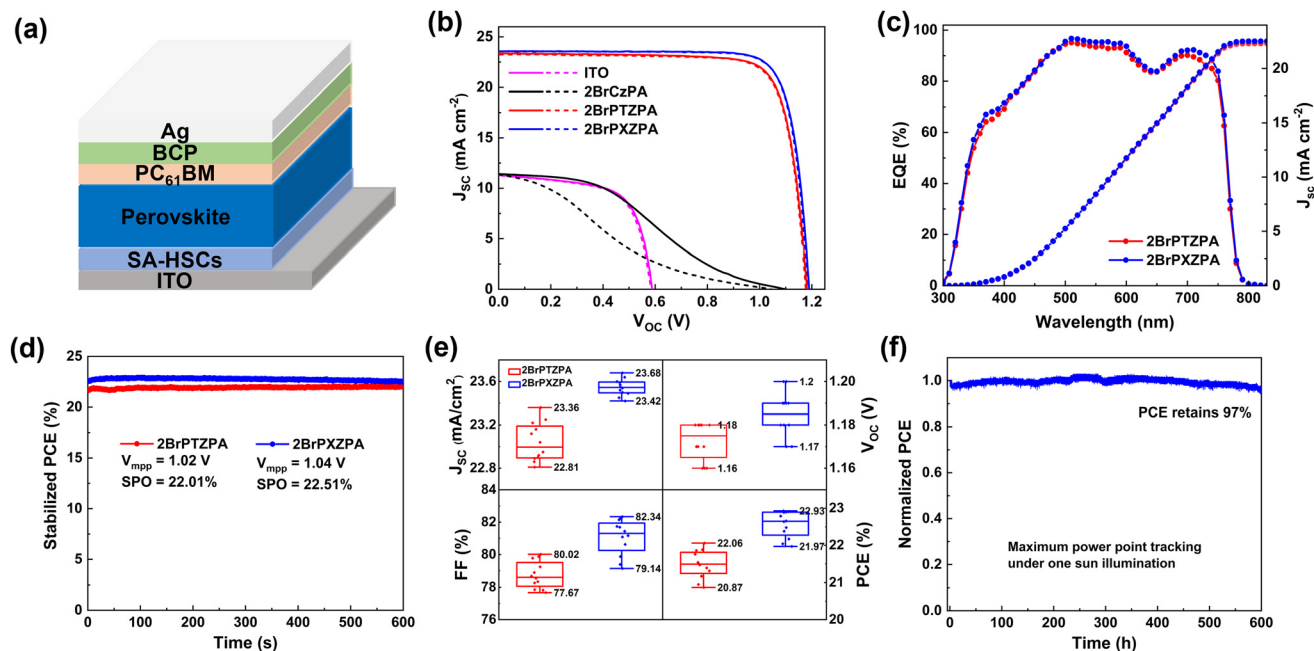
Fig. 3 Photovoltaic performance of PSC devices. (a) Schematic diagram of the inverted PSC device studied in this paper. (b) J–V curves of the best devices based on bare ITO, 2BrCzPA, 2BrPTZPA, and 2BrPXZPA (solid for the reverse scan, short dash for the forward scan). (c) EQE and integrated short-circuit current density of 2BrPTZPA and 2BrPXZPA-based PSC devices. (d) Stabilized PCE for 2BrPTZPA and 2BrPXZPA-based PSC devices at the MPP voltages of 1.02 V and 1.04 V, respectively. (e) Statistic device parameters of 12 devices using 2BrPTZPA and 2BrPXZPA as SA-HSCs. (f) Long-term stability of the 2BrPXZPA-based device.

Table 2 Device performance parameters of the best-performing PSCs with bare ITO, 2BrCzPA, 2BrPTZPA, and 2BrPXZPA as SA-HSCs

SA-HSCs	$J_{sc}{}^a$ (mA cm^{-2})	$J_{sc}{}^b$ (mA cm^{-2})	V_{oc} (V)	FF (%)	PCE (%)
ITO	11.41	—	0.58	65.96	4.37
2BrCzPA	11.43	—	1.10	33.77	4.24
2BrPTZPA	23.36 (23.04 ± 0.18)	22.29	1.18 (1.17 ± 0.01)	80.02 (78.75 ± 0.82)	22.06 (21.48 ± 0.37)
2BrPXZPA	23.59 (23.55 ± 0.08)	22.51	1.19 (1.18 ± 0.01)	81.69 (81.07 ± 1.10)	22.93 (22.56 ± 0.35)

^{a} The statistic values in parentheses obtained from 12 devices. ^{b} The integrated current density estimated from EQE.

PCEs than the PTAA-based devices. However, the 2BrCzPA-based PSC device showed very poor performance with a J_{sc} of 11.43 mA cm^{-2}, a V_{oc} of 1.10 V, and a FF of 33.77%, leading to the lowest PCE of 4.24% in the reverse scan. The much poor photovoltaic performance of 2BrCzPA compared to that of the other two molecules was mainly because of the unmatched interface energy level, as shown in Fig. S8b.† The VBM of the perovskite was higher than the WF of the ITO-modified with 2BrCzPA, which would generate a hole extraction energy barrier and make the hole extraction process more difficult. Holes accumulated at the interface and recombined with electrons leading to low short current density and poor photovoltaic performance.

To confirm the reliability of J–V curves, the external quantum efficiency (EQE) was measured and is shown in Fig. 3c. The integrated current densities of 2BrPTZPA and 2BrPXZPA-based devices were 22.29 and 22.51 mA cm^{-2}, respectively, which were in good agreement with the J–V

measurements. The steady output efficiency of 2BrPTZPA and 2BrPXZPA-based PSCs were recorded with voltage at the maximum power point (MPP, 1.02 and 1.04 V for 2BrPTZPA and 2BrPXZPA, respectively) were 22.01% and 22.51%, respectively, after 600 s, (Fig. 3d) indicating high reliability of the corresponding J–V curves. The reproducibility of 2BrPTZPA and 2BrPXZPA-based devices was further studied. The statistical parameters of the performance of 12 devices are shown in Fig. 3e and Table 2, both the 2BrPTZPA and 2BrPXZPA-based devices showed good reproducibility. The long-term stability of the 2BrPXZA-based device at a maximum power point was evaluated, as shown in Fig. 3f, the PCE retained ∼ 97% of the initial efficiency after 600 h, indicating excellent long-term stability.

To further understand the effect of SA-HSCs on perovskite films, X-ray diffraction (XRD) was carried out and the data is shown in Fig. 4a. The relative intensity of PbI$_2$ compared with the (001) plane was 53.9% for the perovskite film coated on
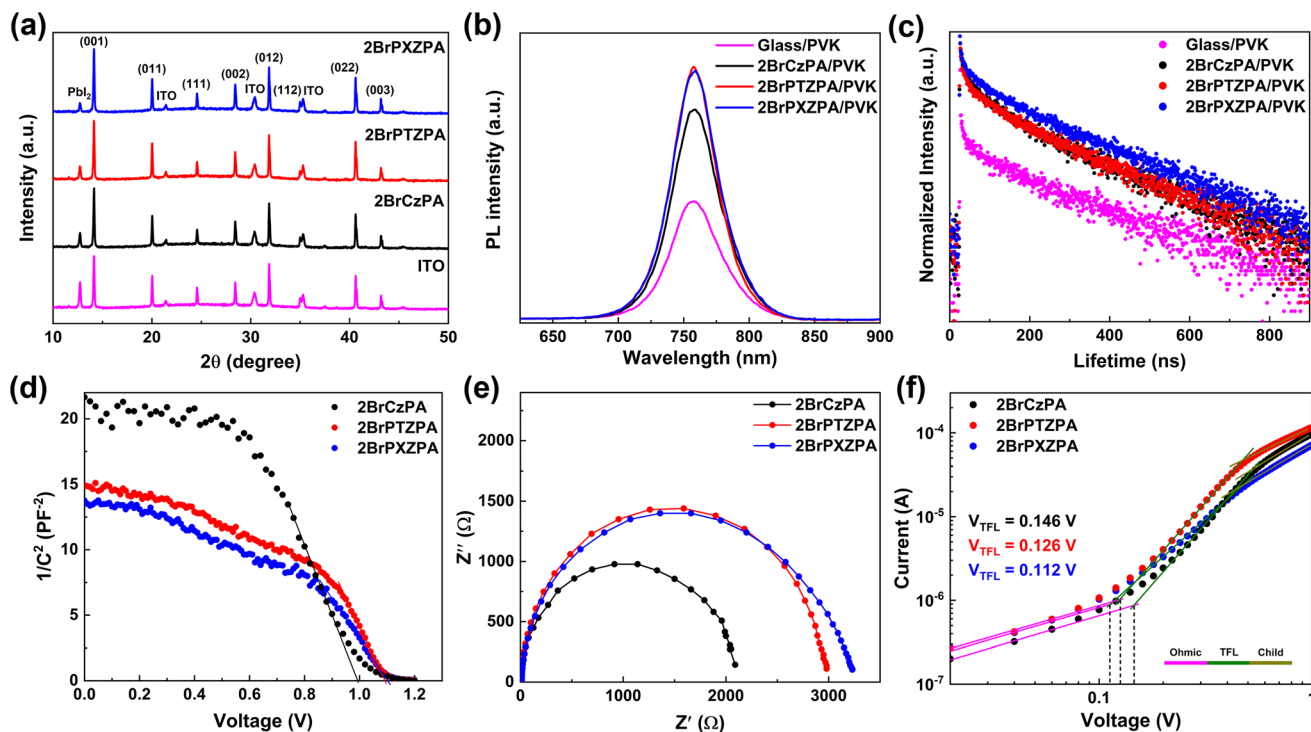
Fig. 4 (a) XRD patterns of perovskite films on different substrates. (b) Steady-state PL spectra and (c) time-resolved PL spectra of perovskite film coated on bare glass, 2BrCzPA, 2BrPTZPA, and 2BrPXZPA. (d) Mott–Schottky plots of PSC devices based on 2BrCzPA, 2BrPTZPA, and 2BrPXZPA. (e) Nyquist plots of PSC devices based on 2BrCzPA, 2BrPTZPA, and 2BrPXZPA. (f) J–V curves of hole-only devices measured for trap state density by the SCLC method with a device configuration of ITO/NiO$_x$/SA-HSCs/perovskite/spiro-OMeTAD/Au.

ITO, indicating that the PbI$_2$ component in the precursor was not efficiently converted into perovskite crystals. After coating on the SA-HSCs, the high-quality perovskite film with the relative intensity of PbI$_2$ decreased to 30.5%, 28.9%, and 20.7% for 2BrCzPA, 2BrPTZPA, and 2BrPXZPA, respectively. In addition, the steady-state and time-resolved photoluminescence (TRPL) measurements were also performed to evaluate the perovskite films, as shown in Fig. 4b and c. Compared with perovskite on bare glass, the improved PL intensity provided evidence that SA-HSCs help suppress nonradiative recombination by reducing the defect sites. The PL lifetime was fitted using a bi-exponential function, as shown in Table S5.† As we know, the fast decay component (τ_1) and the slow decay component (τ_2) were relevant to the defect-induced recombination and radiative recombination of the perovskite film. The perovskite film deposited on the bare glass exhibited a τ_1 of 0.51 ns, a τ_2 of 39.41 ns, and an average lifetime (τ_{ave}) of 22.86 ns, indicating serious recombination decay. After coating SA-HSCs on bare glass, the 2BrCzPA/perovskite, 2BrPTZPA/perovskite, and 2BrPXZPA/perovskite films showed longer decay processes with a τ_{ave} of 112.01 ns, 137.71 ns, and 168.78 ns, respectively, which meant that the defect-induced and radiative recombinations were effectively restrained.

Apart from the photoluminescence property, the electronic property of the device also reflects the charge extraction and recombination process at the interface. In this work, the capacitance–voltage (C–V) and electrical impedance spec-

troscopy (EIS) measurements were performed to evaluate the electronic properties of the PSC devices. The C^{-2}–V plots of 2BrPTZPA and 2BrPXZPA-based devices are shown in Fig. 4d, and the built-in potentials (V_{bi}) were estimated according to the Mott–Schottky equation:

$$C^{-2} = 2(V_{bi} - V)/(A^2 e\varepsilon\varepsilon_0 N_A)$$

where C is the depletion-layer capacitance, V is the applied external voltage, A is the active area, e is the elementary charge, ε and ε_0 are the relative dielectric constant of the perovskite and vacuum dielectronic constant, respectively, and N_A is the carrier density. When C^{-2} is at zero, the applied external voltage equals the build-in potential, so the V_{bi} of 2BrCzPA, 2BrPTZPA, and 2BrPXZPA-based devices was estimated to be 0.99, 1.09, and 1.11 V. The higher V_{bi} could provide a stronger driving force for charge separation and affect the V_{oc} of PSC devices. In addition, the EIS was a powerful method to analyze the charge transport and recombination resistances at the SA-HSCs/perovskite interface. The Nyquist plots of PSC devices based on the three SA-HSCs are shown in Fig. 4e, which was fitted by an equivalent circuit model (ECM) containing a series resistance (R_s) and recombination resistance (R_{rec}). The ECM and fitting parameters are shown in Fig. S16 and Table S6.† The R_s of PSC devices based on 2BrCzPA, 2BrPTZPA, and 2BrPXZPA were 7.9 Ω, 13.3 Ω, and 12.5 Ω, respectively. Nevertheless, the R_{rec} of devices with 2BrCzPA, 2BrPTZPA, and
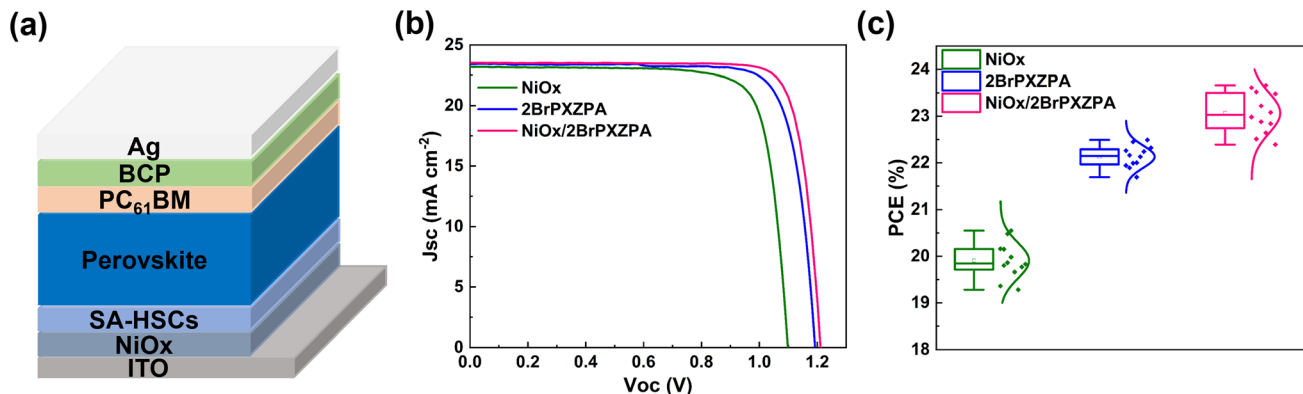
Fig. 5 (a) Schematic diagram of inverted PSC device based on NiO_x/SA-HSCs bilayer. (b) $J-V$ curves of the champion PSC devices and (c) the statistical PCE of PSC devices with different HSCs.

2BrPXZPA increased from 2029 Ω to 2906 Ω and 3112 Ω, which demonstrated that the charge recombination rate was gradually decreased and hence resulted in more efficient charge extraction and larger FF.[48]

To investigate the defect state density in the perovskite film, the hole-only devices with the configuration of ITO/SA-HSCs/CsFAMA/spiro-OMeTAD/Au were fabricated and the $J-V$ curves were plotted, as shown in Fig. 4f. The ohmic region, trap-filled limited (TFL) region and child region could be clearly distinguished from low bias to high bias. The trap state density (n_{trap}) could be calculated with the function:

$$n_{trap} = 2\varepsilon\varepsilon_0 V_{TFL}/eL^2$$

where ε is the relative dielectric constant of perovskite (typically 30 for CaFAMA perovskite),[14] ε_0 is the vacuum permittivity, V_{TFL} is the onset voltage of the TFL region, e is the elementary charge, and L is the thickness of the perovskite films. The V_{TFL} obtained from the $J-V$ curves for 2BrCzPA, 2BrPTZPA and 2BrPXZPA-based devices were 0.146 V, 0.126 V, and 0.112 V, respectively. The corresponding n_{trap} values were calculated as 1.54×10^{15}, 1.34×10^{15}, and 1.18×10^{15} cm^{-3}, respectively, indicating a better defect passivation of 2BrPXZPA. These measurement results were also supported by SEM, which showed that the perovskite deposited on 2BrPXZPA had larger size crystal grains and fewer grain boundaries in the vertical direction than that of 2BrPTZPA.

For inverted PSC devices, NiO_x was widely used as an HSM because of its robust chemical stability, excellent optical transmittance, and low cost. However, high trap density and mismatching of energy level with perovskite suppressed the photovoltaic performance. In this work, the surface of the NiO_x layer was modified with 2BrPXZPA to form an inorganic–organic bilayer HSC, as shown in Fig. 5a. The $J-V$ curves and performance parameters are shown in Fig. 5b and Table 3. The champion PSC device based on NiO_x HSC realized a PCE of 20.55%, with a J_{sc} of 23.23 mA cm^{-2}, a FF of 80.42%, and a V_{oc} of 1.10 V. The relatively poor performance is mainly due to the lower V_{oc}, resulting from the mismatching energy levels between NiO_x and perovskite. Encouragingly, the PSC device

Table 3 Device performance parameters of PSCs with different HSCs

HTLs	J_{sc} (mA cm^{-2})	V_{oc} (V)	FF (%)	PCE^a (%)
NiO_x	23.23	1.10	80.42	20.55 (19.91 ± 0.39)
2BrPXZPA	23.40	1.19	80.76	22.49 (22.13 ± 0.24)
NiO_x/2BrPXZPA	23.52	1.21	82.45	23.66 (23.07 ± 0.44)

^{a} The statistic PCE values were obtained from 12 devices.

with NiO_x/2BrPXZPA bilayer HSC achieved much better performance with a PCE of 23.66%, a J_{sc} of 23.52 mA cm^{-2}, a FF of 82.45%, and a V_{oc} of 1.21 V, which was also higher than that of 2BrPXZPA-based devices. Compared with the NiO_x and 2BrPXZPA-based devices, the excellent PCE of the bilayer HSC-based device was mainly beneficial from its higher V_{oc} and FF. On the one hand, 2BrPXZPA with a deep HOMO energy level would reduce the energy offset between HSC and perovskite. On the other hand, 2BrPXZPA with a phosphoric acid anchoring group bonded with NiO_x would passivate its surface defects and minimize the V_{oc} loss at the interface. The device reproducibility of PSCs based on different HSCs is shown in Fig. 5c, all three kinds of devices had narrow PCE distributions and the average PCE followed the same trend, corresponding to the winning devices. The above results well confirmed that the inorganic–organic bilayer HSC strategy will further improve the photovoltaic performance of the inverted PSCs.

4. Conclusions

In summary, we designed and synthesized three simple and robust self-assembled hole selective materials, *e.g.* 2BrCzPA, 2BrPTZPA, and 2BrPXZPA with butyl spacer linker and Br grafted as the side group in a facile and efficient synthetic procedure. In contrast to 2BrCzPA, by doping O and S in the Cz backbone, 2BrPXZPA and 2BrPTZPA benefitted from the stronger electron-donating property, nonplanar configurations, and lone pair electrons of PTZ and PXZ, the devices based on

2BrPTZPA and 2BrPXZPA with more matched energy alignment, reduced charge recombination loss, and trap density achieving higher PCE of 22.06% and 22.93% (certified PCE of 22.38%), respectively. The 2BrPXZPA-based PSC device exhibited excellent long-term stability with 97% initial efficiency after 600 h one sun AM 1.5G illumination by MPP tracking. In addition, a NiO_x/2BrPXZPA bilayer HSC strategy overcame the high trap density and mismatching of energy-level shortcomings of NiO_x inorganic HSC and achieved a much higher PCE of 23.66% than that of bare NiO_x (20.55%). This work provides an efficient way to reduce the buried interface defects of perovskite and nonradiative recombination energy loss by developing new SA-HSMs with heteroatom doping. Furthermore, this strategy would be a promising choice for large-scale and flexible devices in the future.

Conflicts of interest

The authors declare that they have no known competing financial interests or personal relationships that could have appeared to influence the work reported in this paper.

Acknowledgements

References

1 A. Kojima, K. Teshima, Y. Shirai and T. Miyasaka, *J. Am. Chem. Soc.*, 2009, **131**, 6050–6051.

2 H. Min, D. Y. Lee, J. Kim, G. Kim, K. S. Lee, J. Kim, M. J. Paik, Y. K. Kim, K. S. Kim, M. G. Kim, T. J. Shin and S. Il Seok, *Nature*, 2021, **598**, 444–450.

3 https://www.nrel.gov/pv/assets/pdfs/best-research-cell-efficiencies-rev220630.pdf.

4 L. Meng, J. You, T. F. Guo and Y. Yang, *Acc. Chem. Res.*, 2016, **49**, 155–165.

5 X. Lin, D. Cui, X. Luo, C. Zhang, Q. Han, Y. Wang and L. Han, *Energy Environ. Sci.*, 2020, **13**, 3823–3847.

6 X. Wu, B. Li, Z. Zhu, C. C. Chueh and A. K. Jen, *Chem. Soc. Rev.*, 2021, **50**, 13090–13128.

7 Z. Li, B. Li, X. Wu, S. A. Sheppard, S. Zhang, D. Gao, N. J. Long and Z. Zhu, *Science*, 2022, **376**, 416–420.

8 X. Yin, Z. Song, Z. Li and W. Tang, *Energy Environ. Sci.*, 2020, **13**, 4057–4086.

9 F. Lamberti, F. Schmitz, W. Chen, Z. He and T. Gatti, *Sol. RRL*, 2021, **5**, 2100514.

10 A. Farokhi, H. Shahroosvand, G. D. Monache, M. Pilkington and M. K. Nazeeruddin, *Chem. Soc. Rev.*, 2022, **51**, 5974–6064.

11 W. Chen, F. Liu, X. Feng, A. B. Djurišić, W. K. Chan and Z. He, *Adv. Energy Mater.*, 2017, **7**, 1700722.

12 W. Chen, Y. Wu, J. Fan, A. B. Djurišić, F. Liu, H. W. Tam, A. Ng, C. Surya, W. K. Chan, D. Wang and Z. He, *Adv. Energy Mater.*, 2018, **8**, 1703519.

13 W. Chen, Y. Zhou, L. Wang, Y. Wu, B. Tu, B. Yu, F. Liu, H. W. Tam, G. Wang, A. B. Djurišić, L. Huang and Z. He, *Adv. Mater.*, 2018, **30**, 1800515.

14 W. Chen, G. Pang, Y. Zhou, Y. Sun, F. Liu, R. Chen, S. Chen, A. B. Djurišić and Z. He, *J. Mater. Chem. A*, 2020, **8**, 1865–1874.

15 Y. Wang, L. Duan, M. Zhang, Z. Hameiri, X. Liu, Y. Bai and X. Hao, *Sol. RRL*, 2022, 2200234.

16 F. M. Rombach, S. A. Haque and T. J. Macdonald, *Energy Environ. Sci.*, 2021, **14**, 5161–5190.

17 Y. Xia and S. Dai, *J. Mater. Sci.: Mater. Electron.*, 2020, **32**, 12746–12757.

18 W. Han, G. Ren, J. Liu, Z. Li, H. Bao, C. Liu and W. Guo, *ACS Appl. Mater. Interfaces*, 2020, **12**, 49297–49322.

19 Y. Wang, W. Chen, L. Wang, B. Tu, T. Chen, B. Liu, K. Yang, C. W. Koh, X. Zhang, H. Sun, G. Chen, X. Feng, H. Y. Woo, A. B. Djurišić, Z. He and X. Guo, *Adv. Mater.*, 2019, **31**, 1902781.

20 Y. Cao, W. Chen, H. Sun, D. Wang, P. Chen, A. B. Djurišić, Y. Zhu, B. Tu, X. Guo, B. Tang and Z. He, *Sol. RRL*, 2019, **4**, 1900189.

21 B. Tu, Y. Wang, W. Chen, B. Liu, X. Feng, Y. Zhu, K. Yang, Z. Zhang, Y. Shi, X. Guo, H. F. Li, Z. Tang, A. B. Djurišić and Z. He, *ACS Appl. Mater. Interfaces*, 2019, **11**, 48556–48563.

22 W. Chen, Y. Wang, B. Liu, Y. Gao, Z. Wu, Y. Shi, Y. Tang, K. Yang, Y. Zhang, W. Sun, X. Feng, F. Laquai, H. Y. Woo, A. B. Djurišić, X. Guo and Z. He, *Sci. China: Chem.*, 2020, **64**, 41–51.

23 A. Magomedov, A. Al-Ashouri, E. Kasparavičius, S. Strazdaite, G. Niaura, M. Jošt, T. Malinauskas, S. Albrecht and V. Getautis, *Adv. Energy Mater.*, 2018, **8**, 1801892.

24 A. Al-Ashouri, A. Magomedov, M. Roß, M. Jošt, M. Talaikis, G. Chistiakova, T. Bertram, J. A. Márquez, E. Köhnen, E. Kasparavičius, S. Levcenco, L. Gil-Escrig, C. J. Hages, R. Schlatmann, B. Rech, T. Malinauskas, T. Unold, C. A. Kaufmann, L. Korte, G. Niaura, V. Getautis and S. Albrecht, *Energy Environ. Sci.*, 2019, **12**, 3356–3369.

25 A. Al-Ashouri, E. Kohnen, B. Li, A. Magomedov, H. Hempel, P. Caprioglio, J. A. Marquez, A. B. Morales Vilches, E. Kasparavicius, J. A. Smith, N. Phung, D. Menzel, M. Grischek, L. Kegelmann, D. Skroblin, C. Gollwitzer, T. Malinauskas, M. Jost, G. Matic, B. Rech, R. Schlatmann, M. Topic, L. Korte, A. Abate, B. Stannowski, D. Neher, M. Stolterfoht, T. Unold, V. Getautis and S. Albrecht, *Science*, 2020, **370**, 1300–1309.

26 L. Li, Y. Wang, X. Wang, R. Lin, X. Luo, Z. Liu, K. Zhou, S. Xiong, Q. Bao, G. Chen, Y. Tian, Y. Deng, K. Xiao, J. Wu, M. I. Saidaminov, H. Lin, C.-Q. Ma, Z. Zhao, Y. Wu, L. Zhang and H. Tan, *Nat. Energy*, 2022, **7**, 708–717.

27 W. Chen, Y. Zhu, J. Xiu, G. Chen, H. Liang, S. Liu, H. Xue, E. Birgersson, J. W. Ho, X. Qin, J. Lin, R. Ma, T. Liu, Y. He, A. M.-C. Ng, X. Guo, Z. He, H. Yan, A. B. Djurišić and Y. Hou, *Nat. Energy*, 2022, **7**, 229–237.

28 H. Tian, X. Yang, R. Chen, Y. Pan, L. Li, A. Hagfeldt and L. Sun, *Chem. Commun.*, 2007, 3741–3743.

29 A. F. Buene and D. M. Almenningen, *J. Mater. Chem. C*, 2021, **9**, 11974–11994.

30 J. Lee, K. Shizu, H. Tanaka, H. Nomura, T. Yasuda and C. Adachi, *J. Mater. Chem. C*, 2013, **1**, 4599–4604.

31 H. Tanaka, K. Shizu, H. Miyazaki and C. Adachi, *Chem. Commun.*, 2012, **48**, 11392–11394.

32 D. Chen, P. Rajamalli, F. Tenopala-Carmona, C. L. Carpenter-Warren, D. B. Cordes, C. M. Keum, A. M. Z. Slawin, M. C. Gather and E. Zysman-Colman, *Adv. Opt. Mater.*, 2019, **8**, 1901283.

33 M. Cheng, C. Chen, X. Yang, J. Huang, F. Zhang, B. Xu and L. Sun, *Chem. Mater.*, 2015, **27**, 1808–1814.

34 Y. Chen, X. Xu, N. Cai, S. Qian, R. Luo, Y. Huo and S. W. Tsang, *Adv. Energy Mater.*, 2019, **9**, 1901268.

35 N. Cai, F. Li, Y. Chen, R. Luo, T. Hu, F. Lin, S. M. Yiu, D. Liu, D. Lei, Z. Zhu and A. K. Jen, *Angew. Chem., Int. Ed.*, 2021, **60**, 20437–20442.

36 E. Li, C. Liu, H. Lin, X. Xu, S. Liu, S. Zhang, M. Yu, X. M. Cao, Y. Wu and W. H. Zhu, *Adv. Funct. Mater.*, 2021, **31**, 2103847.

37 A. Ullah, K. H. Park, H. D. Nguyen, Y. Siddique, S. F. A. Shah, H. Tran, S. Park, S. I. Lee, K. K. Lee, C. H. Han, K. Kim, S. Ahn, I. Jeong, Y. S. Park and S. Hong, *Adv. Energy Mater.*, 2021, 2103175.

38 R. Li, C. Li, M. Liu, P. Vivo, M. Zheng, Z. Dai, J. Zhan, B. He, H. Li, W. Yang, Z. Zhou and H. Zhang, *CCS Chem.*, 2021, 3309–3319.

39 W. Chen, B. Han, Q. Hu, M. Gu, Y. Zhu, W. Yang, Y. Zhou, D. Luo, F. Liu, R. Cheng, R. Zhu, S. Feng, A. B. Djurišić, T. P. Russell and Z. He, *Sci. Bull.*, 2021, **66**(10), 991–1002.

40 K. Yang, Q. Liao, J. Huang, Z. Zhang, M. Su, Z. Chen, Z. Wu, D. Wang, Z. Lai, H. Y. Woo, Y. Cao, P. Gao and X. Guo, *Angew. Chem., Int. Ed.*, 2022, **61**, 202113749.

41 L. Xu, D. Wu, W. Lv, Y. Xiang, Y. Liu, Y. Tao, J. Yin, M. Qian, P. Li, L. Zhang, S. Chen, O. F. Mohammed, O. M. Bakr, Z. Duan, R. Chen and W. Huang, *Adv. Mater.*, 2022, **34**, 2107111.

42 A. Asyuda, M. Gärtner, X. Wan, I. Burkhart, T. Saßmannshausen, A. Terfort and M. Zharnikov, *J. Phys. Chem. C*, 2020, **124**, 8775–8785.

43 N. Singh, A. Mohapatra, C.-W. Chu and Y.-T. Tao, *Org. Electron.*, 2021, **98**, 106297.

44 Y. Lin, A. Magomedov, Y. Firdaus, D. Kaltsas, A. El-Labban, H. Faber, D. R. Naphade, E. Yengel, X. Zheng, E. Yarali, N. Chaturvedi, K. Loganathan, D. Gkeka, S. H. AlShammari, O. M. Bakr, F. Laquai, L. Tsetseris, V. Getautis and T. D. Anthopoulos, *ChemSusChem*, 2021, **14**, 3569–3578.

45 J. A. Bardecker, H. Ma, T. Kim, F. Huang, M. S. Liu, Y.-J. Cheng, G. Ting and A. K. Y. Jen, *Adv. Funct. Mater.*, 2008, **18**, 3964–3971.

46 S. Khodabakhsh, D. Poplavskyy, S. Heutz, J. Nelson, D. D. C. Bradley, H. Murata and T. S. Jones, *Adv. Funct. Mater.*, 2004, **14**, 1205–1210.

47 S. Khodabakhsh, B. M. Sanderson, J. Nelson and T. S. Jones, *Adv. Funct. Mater.*, 2006, **16**, 95–100.

48 A. Fakharuddin, L. Schmidt-Mende, G. Garcia-Belmonte, R. Jose and I. Mora-Sero, *Adv. Energy Mater.*, 2017, **7**, 1700623.